

PAPER

Full-orbit and drift calculations of fusion product losses due to explosive fishbones on JET

To cite this article: M. Fitzgerald *et al* 2019 *Nucl. Fusion* **59** 016004

View the [article online](#) for updates and enhancements.

Full-orbit and drift calculations of fusion product losses due to explosive fishbones on JET

M. Fitzgerald, J. Buchanan, S.E. Sharapov[✉], V.G. Kiptily, M. Sertoli, G. Szepesi, J. Boom, R.J. Akers, D. King and JET contributors^a

EUROfusion Consortium, JET, Culham Science Centre, Abingdon, OX14 3DB, United Kingdom of Great Britain and Northern Ireland

E-mail: Michael.Fitzgerald@ukaea.uk

Received 20 August 2018, revised 2 October 2018

Accepted for publication 22 October 2018

Published 14 November 2018



Abstract

Fishbones are ubiquitous in high-performance JET plasmas and are typically considered to be unimportant for scenario design. However, during recent high-performance hybrid scenario experiments, sporadic and explosive fishbone oscillations with sawtooth reconnection were observed coinciding with reduced performance and a main chamber hotspot. Fast ion loss diagnostics showed fusion products ejected from the plasma by the fishbones. We present calculations of the perturbed motion of non-resonant fusion products in the presence of fishbones assuming a fixed linear mode structure and frequency. Using careful reconstruction of the equilibrium and measurements of the perturbation, we show that the measured fishbone spatial structure in these experiments can be well modelled as a linear MHD internal kink mode. Both drift and full-orbit calculations predict losses of fusion products at the same location of the observed hotspot, however the calculated energy content of those losses is negligible and cannot be contributing significantly. The fast ions responsible for the hotspot and the reason for their loss both remain unexplained.

Keywords: fishbone, sawteeth, fusion products, losses, JET, fast particles, instability

(Some figures may appear in colour only in the online journal)

Introduction

The hybrid scenario on the JET tokamak is being developed to achieve long pulses at high performance in future deuterium–tritium experiments [1]. The scenario is characterised both by a safety factor q close to unity at the magnetic axis as well as low magnetic shear $\frac{r}{q} \frac{dq}{dr}$. The combination of high thermal pressure and weak magnetic stabilization makes the configuration susceptible to instability. Neoclassical tearing modes (NTMs) are often observed to degrade the fusion yields in JET hybrid scenarios, requiring fine adjustments in scenario design for each attempt at high fusion power to avoid them. Explosive fishbone oscillations are also observed due to the

presence of energetic particles from neutral beam and radio frequency heating. During recent hybrid experiments, fishbones are clearly responsible for fusion product losses [2, 3], but perhaps more concerning is the presence of main chamber hot-spots which can force termination of the experiment in order to protect the in-vessel components. A key question is whether the observed fishbones are causing sufficient numbers of fast ions to be ejected resulting in hotspots.

In scenarios with a safety factor below $q = 1$, the sawtooth instability occurs with an $n = 1$ toroidal and predominantly $m = 1$ poloidal ‘kink’ spatial periodicity. Maintaining the safety factor at or above unity is effective in preventing the sawtooth instability, and the presence of fast particles contributes a bounce/transit orbit-sized magnetic moment which also tends to stabilize this kink instability for $q < 1$ [4]. However, the characteristic precessional times of the tens of keV

^a See the author list of Litaudon *et al* [25].

trapped fast particle orbits become resonant with an oscillatory version of the kink mode, meaning that the very same fast particles that stabilize the sawtooth instability can excite a fishbone oscillation [5–7].

Although sharing a similar kink spatial profile to the sawtooth and other ‘1/1 activity’, the fishbone oscillation is distinct in that it exhibits a real wave frequency in the plasma frame. This real frequency induces an electric field and alters the wave-particle resonance condition from that for the zero-frequency tearing-modes. Furthermore, the fishbone is not merely an eigenmode of the bulk thermal plasma excited by fast particles, but rather an energetic particle mode, where the coherent motion of the fast particles themselves comprise part of the mode.

For a low- β conventional tokamak such as JET, $m = 1$ instabilities in the linear MHD theory resemble the ‘internal kink mode’ which requires a $q = 1$ surface to exist [8]. There is some variation in analytical predictions and terminology for the ideal MHD mode structure depending on the character of the equilibrium profiles, driving mechanism and orderings assumed [9–12], but they share the quality of being bounded by a $q = 1$ surface. We will not explicitly distinguish between any of these specific limiting cases, with terminology used such as ‘quasi-interchange’ mode, but simply refer to all these bounded solutions as internal kink modes. In addition to the internal kink modes, theory also predicts [13] that for sufficiently large β and low magnetic shear, pressure may drive an ‘infernal kink mode’. The significance of the infernal solution is that it describes a perturbation that extends beyond the location of the $q = 1$ surface, with an increased number of poloidal harmonics in its profile. When predicting the radial positions of ion orbits that are affected, correctly choosing between infernal modes and internal modes is likely important. Determining if encountered fishbones appear to require a rational surface also clarifies the required remedy in scenario design.

In this paper, we present detailed calculations of fusion product losses caused by fishbones observed in JET discharge #92394, in order to fully explain the observed fusion product losses and assess their role in the observed hotspots in the same discharge.

Experimental setup and observations of mode activity

The work in this paper focuses on detailed analysis of experimental observations published earlier [2]. Here we repeat key observations as an introduction to our analysis.

We consider a recent good case of the hybrid scenario on JET with ITER-like wall, with equilibrium magnetic field and current $B/I = 2.8$ T/2.2 MA, and $\beta_N \sim 2.6$ (discharge #92394). Figure 1 is a set of plots of the main plasma conditions in this discharge, as well as magnetics and fast ion loss data showing the onset of sporadic large-amplitude fishbones.

Coherent losses at the fishbone frequency are measured on the fast ion loss detector (FILD) [14]. In addition, a main chamber hotspot is evident on an outboard poloidal limiter

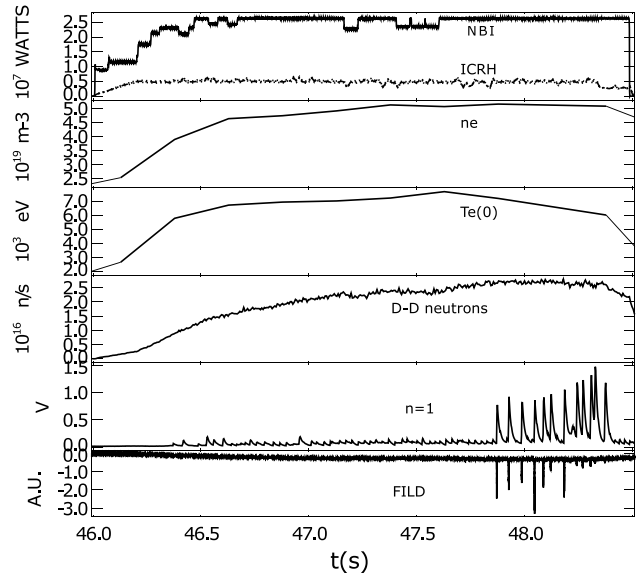


Figure 1. High performance hybrid scenario #92394. From top to bottom: NBI and ICRH power wave-forms; line-averaged electron density measured with interferometry line-of-sight through the magnetic axis; electron temperature measured with ECE on the magnetic axis; D–D neutron rate from fission chambers; $n = 1$ MHD activity; fast ion loss detector signal.

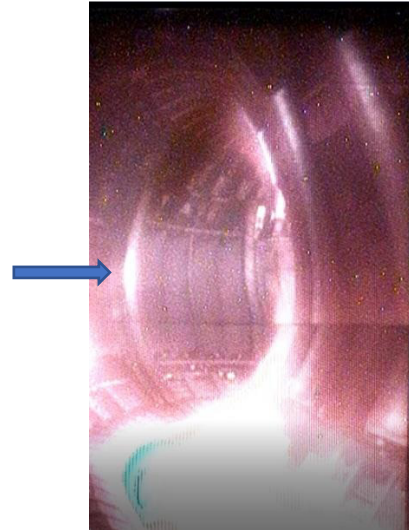


Figure 2. Visible camera frame taken during fishbone activity for discharge #92394. A hotspot is evident on an outboard poloidal limiter, indicated with the arrow.

(figure 2). The hotspot was sufficiently intense as to trigger machine protection systems and terminate the pulse.

After subtracting the FILD loss signal before fishbones from the signal during the fishbones, the maximum fast ion losses are measured to be associated with the pitch-angle at the FILD $\theta \equiv \cos^{-1} \frac{v \cdot B}{|v||B|}$ of 55° and Larmor radii of 8–13 cm (figure 3). If one assumes that ICRH accelerated hydrogen minority ions satisfy the fundamental resonance condition $\omega - k_{\parallel}v - \Omega_c(x) = 0$, and that resonant ICRH particles spend the most time in resonance when $v_{\parallel} = 0$, then the majority of ICRH accelerated minority ions will follow orbits with banana tips occurring near the resonance line in figure 4, and

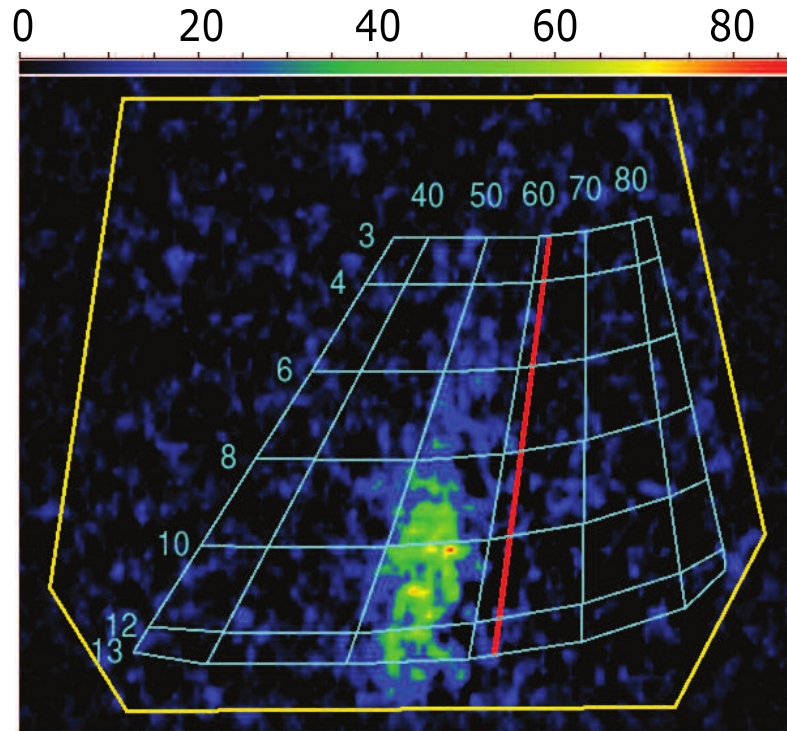


Figure 3. FILD data from discharge #92394 showing fast ion losses as functions of the pitch-angles in the range 40° – 80° and Larmor radii 3 cm–13 cm. Only the difference in signal with and without fishbones is shown. The pitch-angle corresponding to the ICRH H-minority fast ions is shown in solid red. Reproduced courtesy of IAEA. Figure from [2]. © EURATOM 2017.

have a distribution in pitch which is roughly Gaussian around this resonance. These fishbone-correlated losses are therefore unlikely to be associated with the ICRH-accelerated hydrogen (H) minority ions; ICRH resonance orbits correspond to pitch-angles near 63° (shown with red line). Although we cannot make conclusions regarding ICRH losses below ~ 600 keV (protons) or ~ 300 keV (deuterons) on the FILD (or their potential role in hotspots), the complete absence of lower energy particles on the FILD suggests that no ICRH tail is being observed at these energies and all particles measured on the FILD are starting at high energies before being promptly lost.

Backwards full-orbit modelling (figure 4) shows that the losses detected are associated with the highly energetic D–D fusion products (3 MeV protons and 1 MeV tritons), not with H minority ions. The fusion products are lost mostly from the high-field side region of the plasma, close to the trapped-passing boundary. Small differences in measured pitch angle at the FILD imply large differences in the banana tip positions of the orbits (shown explicitly in [2] but omitted here).

Equilibrium reconstruction and predicted mode structure

Equilibrium reconstruction using the EFIT code on JET typically requires the use of internal constraints such as Faraday

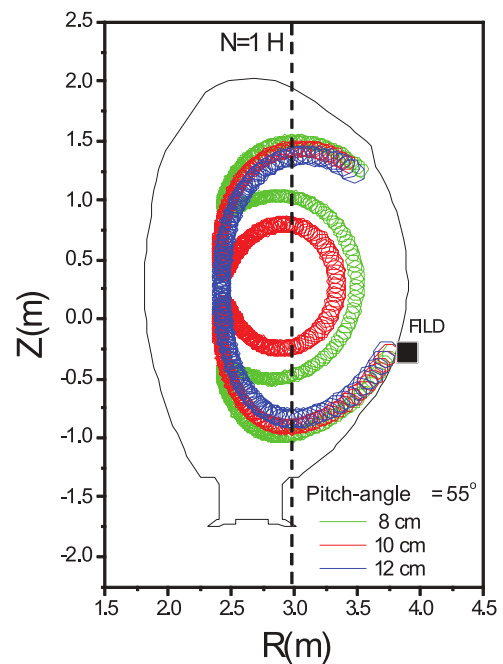


Figure 4. Full-orbit ‘backward’ modelling for fast ion losses at the position of fast ion lost detector (FILD). The approximate location of the fundamental H-minority ICRH resonance is shown with the dashed line. Reproduced courtesy of IAEA. Figure from [2]. © EURATOM 2017.

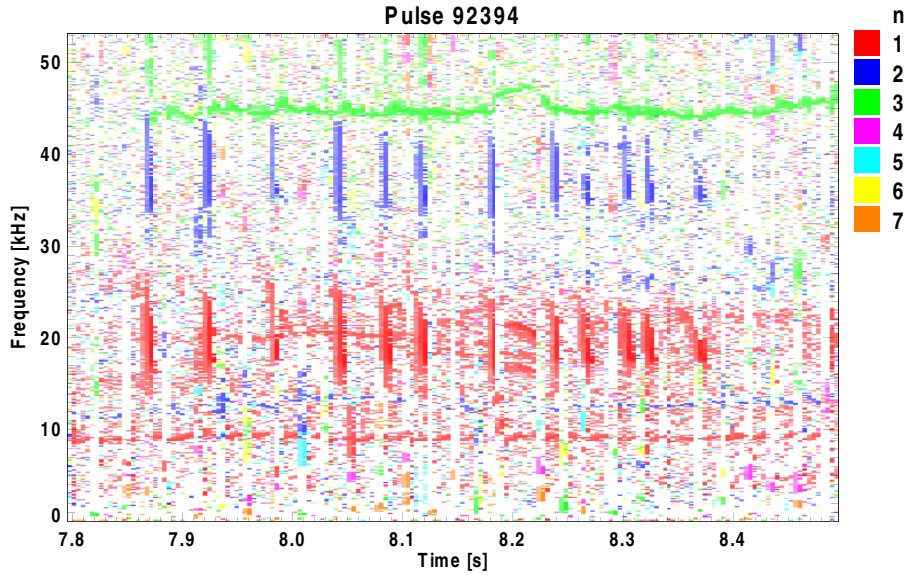


Figure 5. Fourier spectrogram taken from fast magnetics, with modes coloured by inferred toroidal mode number.

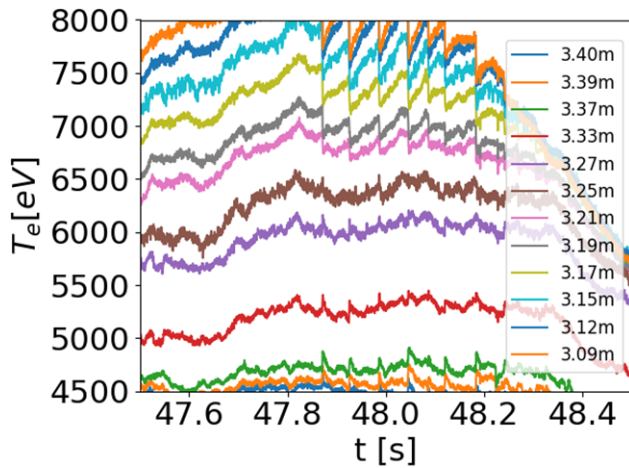


Figure 6. Electron temperature time-traces measured through electron cyclotron emission at radial locations around the sawtooth inversion radius. Temperature decreases with increasing major radius. Discharge #92394.

rotation, motional Stark effect and pressure [15] if the q profile is to be used for stability analysis. Even with those internal constraints, in the hybrid scenario, the low shear in the core would imply an unfavourably large uncertainty in the inferred position of the $q = 1$ rational surface for any EFIT reconstruction. The tactic employed in this study to reduce the uncertainty in safety factor was to further constrain the equilibrium using measurements of MHD markers. For example, it is well known that tearing modes occur at locations where $q = m/n$. Figure 5 is a Fourier spectrogram coloured by toroidal mode number. The relevant MHD markers evident in this plot are a $4/3$ NTM at ~ 45 kHz and a $2/1$ mode at ~ 8 kHz.

The most important additional MHD marker in the case that we present here is the $q = 1$ sawtooth inversion radius in electron temperature, as measured through electron cyclotron

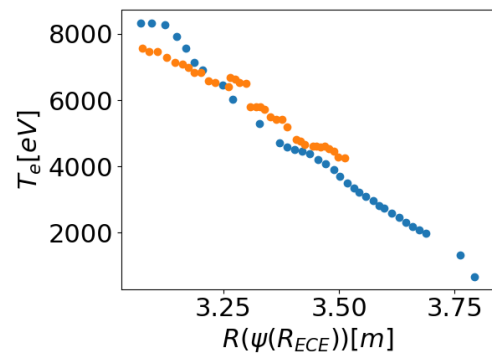


Figure 7. Calibrated ECE radial profile of electron temperature versus flux label. The flux label is expressed as a radial position on the outboard midplane. Note the plasma boundary is at approximately 3.8 m. Orange denotes measurements on the high-field side. Discharge #92394.

emission (ECE). Figure 6 contains plots of the time-trace of electron temperature for a set of radial channels. Distinctive sawtooth-like drops in temperature around $R = 3.2$ m are simultaneous with rises in temperature at $R = 3.3$ m, confirming field reconnection and the interpretation of sawteeth. The intense fishbones that are observed on the magnetics are simultaneous with the observed sawteeth, indicating a hybrid fishbone-sawtooth ‘sawbone’ character as first observed on PDX, also with associated fast ion loss [7, 16].

The ECE diagnostic on JET requires knowledge of the local magnetic field in order to calibrate the radial position of the channel. This calibration in turn depends weakly on the equilibrium reconstruction. Convergence in calibrated radial position for this case occurred after a single reprocessing of this consistency loop. The consistency check between equilibrium and ECE was the requirement that electron temperature be a flux function. Figure 7 is a plot comparing the electron temperature measured on the inboard and outboard midplane

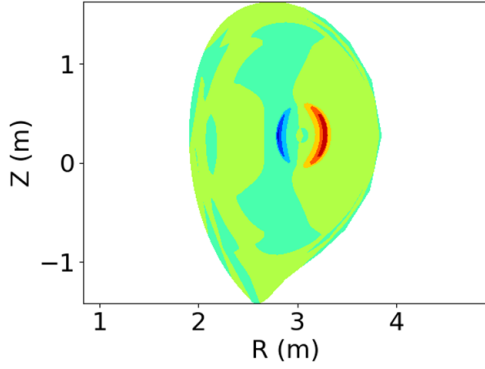


Figure 8. Electrostatic potential of linear MHD internal kink mode used to model the fishbone. The mode is evidently dominated by $m = 1$ but the weak $m = 2$ contributions can also be discerned (dark green structures).

as a function of flux-surface label (outboard major radius was chosen to label the poloidal flux surfaces in the plot). The degree of asymmetry present suggests an error in radial position of ± 2 cm reduced from ± 5 cm in a similar plot before reprocessing.

Clearly evident in figure 7 is the flattening of electron temperature at the location of the aforementioned 4/3 NTM. The location of the tearing mode was confirmed using a cross-correlation technique with fast magnetics [17], detecting a phase shift at the same location, indicative of a magnetic island. The location of the 2/1 mode in figure 5 was also confirmed using the same technique.

The three locations obtained from MHD markers, 3.25 ± 0.02 m for sawtooth inversion, 3.42 ± 0.02 m for the 4/3 and 3.65 ± 0.05 m for the 2/1 modes, constrained the value of safety factor at those locations to be $q = 1, 1.33, 2.0$ respectively. EFIT was re-run with the usual internal constraints, but with particular care to satisfy the measured q constraints. Even when using the usual internal constraints, some freedom still remains with EFIT reconstruction in specifying the prior assumptions for allowed forms of the plasma current or for the relative weights of various measurements. To manually obtain a q profile that agrees with the measured values, we exploited this ambiguity by adjusting the relative weighting factor of the imposed internal pressure constraint by $\sim 20\%$ until a satisfactory match with MHD constraints was obtained.

Assumed form for the fishbone

Using the MHD marker constrained equilibrium for shot #92394 at 47.8 s, a stable linear internal kink mode was computed using the ideal MHD MISHKA-1 code [18]. The linear eigenfunctions output from MISHKA-1 represent the perturbed fluid velocity $\tilde{\mathbf{V}}$ for the modes which relate to the perturbed vector potential $\tilde{\mathbf{A}}$

$$\lambda \mathbf{A} = -\mathbf{B}_0 \times \tilde{\mathbf{V}} \quad (1)$$

where λ is the complex eigenvalue of the normal mode that varies in time as $\exp \lambda t$. The electric and magnetic fields for the perturbation are immediately obtained through the definition of the vector potential and Faraday's law

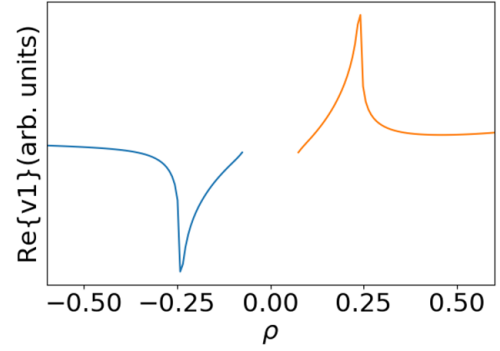


Figure 9. Perturbed radial fluid velocity as computed by MISHKA, summed over poloidal harmonics and remapped onto normalized root toroidal flux ρ (with negative values denoting high field side).

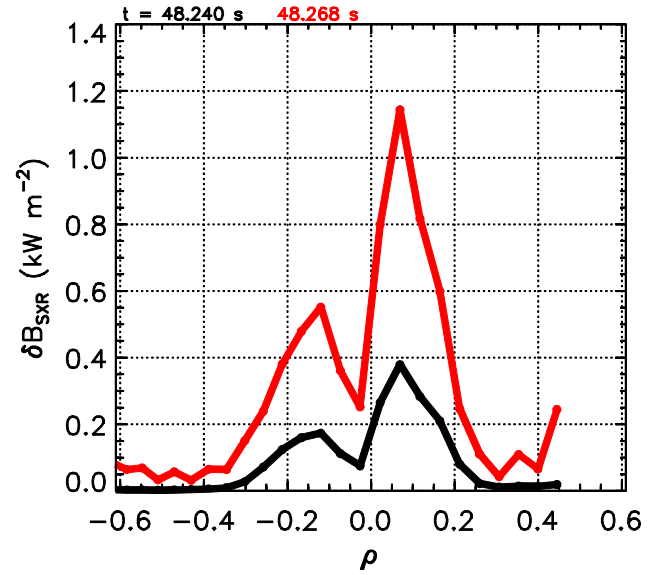


Figure 10. SXR measurements of perturbed intensity as a function of normalized root toroidal flux, taken at two different times during two different fishbones. Discharge #92394.

$$\delta \mathbf{B} = \nabla \times \mathbf{A} \quad (2)$$

$$\delta \mathbf{E} = -\lambda \mathbf{A}. \quad (3)$$

Taking advantage of the small parallel perturbed magnetic field $\delta B_{\parallel} \approx 0$, the electric field may be re-written

$$\delta \mathbf{E} = -\lambda \alpha \mathbf{B}_0 - \nabla \phi \quad (4)$$

where we have introduced the electrostatic potential ϕ and an additional function α . In ideal MHD, $\delta E_{\parallel} = 0$ and the two functions are trivially related through k_{\parallel} . The perpendicular electric field for the linear ideal MHD kink mode is therefore completely visualised in the perpendicular plane by the electrostatic potential.

The resulting eigenmode electrostatic potential for our case is shown in figure 8.

The solution retains up to 20 poloidal harmonics, but it is obvious from the figure that the eigenmode is dominated by $m = 1$. Although it is predicted that fishbones will nonlinearly evolve in mode structure [19, 20], we assume that the nonlinear fishbone mode can be well modelled by the linear MHD

mode to the extent required to predict prompt fast ion losses. In the calculations that follow, we will be assuming large amplitudes for the perturbation which will result in stochastic fast ion motion. Under such circumstances, we expect only the radial extent of the mode to alter conclusions made about particle transport, rather than the detailed mode structure.

Soft x-ray (SXR) measurements of perturbed intensity at the instantaneous fishbone frequency provide line-integrated measurements of the fishbone radial extent. The MISHKA mode structure as a function of normalized toroidal flux at ρ is provided in figure 9 for direct comparison with perturbed intensity in figure 10. Both the prediction and the measurements show a clear boundary for the perturbation at $\rho = 0.3$ on the outboard midplane. The measured and modelled edge of the fishbone structure are in very good agreement, and the shape is somewhat less acute in the measurements as could be expected from the convolution with line-of-sight and equilibrium density effects but could also imply a larger value of shear inside $q = 1$ than our computed equilibrium. Nonlinear theory also predicts a smoothing of the linear fishbone profile [21].

The measured perturbation phase given in figure 11 shows a clear π phase change between inboard and outboard sides confirming the predominant $m = 1$ poloidal structure. This supports the assumption that there is dominance of the $m = 1$ component in the nonlinear phase of the fishbone comparable to the linear internal kink mode.

These SXR measurements rule out the infernal modes predicted by theory as being a good description of the fishbone in this high-performance hybrid experiment. On the contrary, these fishbones do not require vanishing shear and do not exist where $q > 1$.

In the sections that follow, we will show that the localisation of the fishbone within the $q = 1$ surface, as for an internal kink mode, significantly reduces the proportion of particle orbits which may be lost as a result of these fishbones.

Calculation of unperturbed orbits

In order to understand the mechanism of fusion product losses due to the fishbone, it is necessary to first characterise the confined motion of unperturbed orbits, and then describe how that motion changes. Confined orbits in the axisymmetric tokamak may be labelled uniquely by invariants of motion: energy E , magnetic moment μ , toroidal canonical momentum P_ϕ , with an additional parameter $\sigma = \text{sgn}(v_\parallel)$ the sign of the particle velocity parallel with the magnetic field. On JET, the toroidal components of the plasma current and magnetic field are in the same direction (clockwise from above). This is also the same direction as the neutral beams and typical ion diamagnetic drift. For all confined equilibrium orbits, σ is either also an invariant of the motion or, in the case of trapped particles, a redundant label. For this work, we chose a related set of invariants $(E, \Lambda, +Z_{R=R_0}; \sigma)$. The invariant pitch $\Lambda \equiv \frac{\mu B_0}{E}$ where B_0 is the magnetic field at the magnetic axis, is a practical measure of the maximum field encountered by the particle and consequently the minimum value of major radius R .

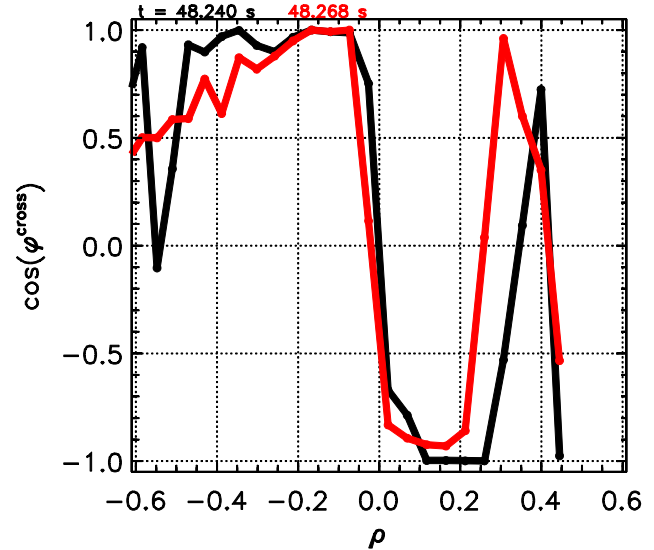


Figure 11. SXR measurements showing phase change of perturbed intensity as a function of normalized root toroidal flux, taken at the same times as the previous figure. Discharge #92394.

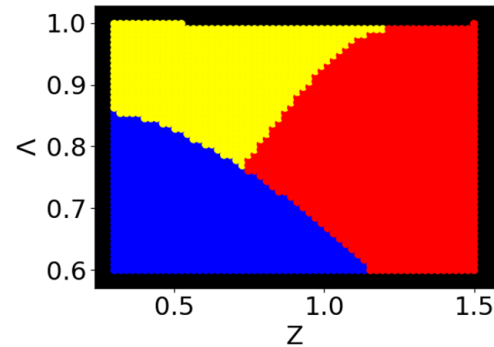


Figure 12. Unperturbed orbit classification as a function of orbit invariants for 3 MeV protons travelling counter-field as calculated with the full-orbit LOCUST code. Blue denotes passing, yellow trapped and red lost.

For example, $\Lambda \equiv 1$ corresponds to particles with perpendicular energy equalling total energy at B_0 , very much like most of the hydrogen minority ICRH particles driven on-axis.

For a given choice of $(E, \Lambda; \sigma)$, an orbit that crosses the Z axis above the magnetic axis will cross in exactly one location depending on the choice of P_ϕ . P_ϕ is not a directly measurable or intuitive label for the fishbone-particle interaction as it mixes velocity and spatial information, and the spatial information is indirect as it involves knowledge of the poloidal flux.

The value of the cylindrical coordinate Z taken directly above the magnetic axis $+Z_{R=R_0}$ is chosen as a more useful choice than P_ϕ for this work, allowing straightforward visualisation of when particle orbits cross the fishbone. In the phase-space plots that follow, we will omit the embellishments in the notation for this invariant and simply write Z .

A number of 1st order drift orbit calculations using the HAGIS guiding-centre code [22] were carried out, and we have already published some results [2]. In addition, we have also recently developed the HALO (HAGIS LOCust) code which takes mode structure from MISHKA in the same manner as HAGIS. HALO tracks the particle motion in full-orbit using

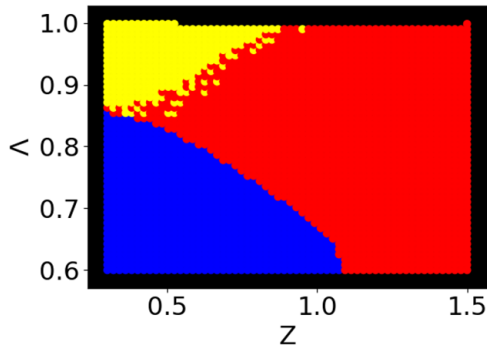


Figure 13. Full-orbit calculation of unperturbed topologies using LOCUST with a wall model. The proximity of the wall to the separatrix results in losses of fusion products even though the guiding centre motion is still confined.

the LOCUST code, allowing tracking even beyond the separatrix until reaching the plasma facing components. The same calculations of fishbone induced losses were carried out with both codes, and differences for our fishbone calculations will be mentioned where significant. Detailed benchmarking of the new HALO code against HAGIS has been carried out but those results are a distraction here, and will be detailed in a subsequent publication.

Figure 12 is a scatter plot in phase space showing the orbit classification for 3 MeV protons travelling counter-field, as a function of the orbit invariants ($+Z_{R=R_0}$, Λ). The topology boundaries between trapped, passing and lost particles meet at a triple-point and this small region of phase space is chosen for the plot. Note that the ICRH resonance line discussed earlier in figure 3 corresponds to $\Lambda = 1$, which are clearly quite different orbits to those on the trapped/passing boundary.

The 3 MeV proton energy chosen is the birth energy for the fusion products in the D–D reaction. Fast triton fusion products at 1 MeV were also measured [2] but follow the same orbits so we will make no more explicit mention of them.

Both HAGIS drift calculations and full-orbit LOCUST calculations using the same guiding-centre locations were carried out. We have chosen to load our particles at fixed gyrophase for comparison between codes. The same results for orbit topologies were obtained and are not shown here. However, the additional physics of full-orbit tracking outside the separatrix allowed the inclusion of a wall model. Figure 13 including the wall model shows that although barely confined guiding centres remain inside the separatrix in the drift model neglecting FLR excursion, the Larmor radius of the fusion products is sufficiently large as to impact the wall on the outboard midplane. The Larmor radius of fusion products encountering the nearby limiter causes a shift in the critical loss triple-point region inwards.

Although the large fishbone amplitudes assumed in our calculations can create significant deviations in particle orbits (further discussion of large amplitude later), when considering losses and hotspots, we are seeking to study deviations which ultimately result in a loss, not merely redistribution in phase space. The omitted low values of Λ in figure 12 have confined counter-passing orbits that transition to loss orbits

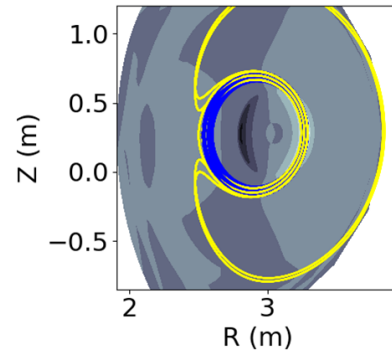


Figure 14. A selection of nine confined unperturbed guiding centre orbits from HAGIS chosen near the triple-point. The orbits are overlaid on a plot of the fishbone electrostatic potential. Blue denotes passing and yellow trapped.

only at large values of Z . The satisfactory confinement of fusion products at low Λ is even better for co-passing ions. Fusion products are overwhelmingly not produced at regions of high Z , and even if they were, the fishbone that we are studying has been demonstrated to exist only at small values of Z . In a drift picture, the magnetic moment of the particles is invariant, so variations in Λ will be small due to the fishbone. It is therefore clear that to explain any losses at all we must study the critical region of phase space around the triple-point given in figure 12.

A selection of HAGIS confined drift orbits near the critical triple-point region is shown in figure 14. Small changes in radius or pitch change the orbit topology from counter-passing to trapped. This radically changes the time-average position of core localised particles due to the large orbit width. At these values of Z , the orbits are also barely confined if not lost. It is notable that barely confined fusion products are most likely to be lost along the midplane, with wall impacts occurring further below the midplane for particles deeper in the loss region of phase space. As well as showing the particle orbits, figure 14 also shows the perturbed electrostatic potential encountered by the critical orbits. The guiding centres of the critical orbits match almost perfectly with the location of the fishbone, indicating that those particles which are the most likely to be lost due to a topology change happen to be precisely the same particles which enter regions with the strongest perturbing fields. A loss orbit must encounter both the $q = 1$ surface and the plasma boundary, so the figure makes it immediately evident that orbits with significantly lower energy and smaller orbit-width than these fusion products cannot be lost because of fishbones alone.

Having established the nature of unperturbed orbits which are the most likely to be lost due to interaction of a fishbone, in the next section we will present the calculations of orbits with the inclusion of the perturbing fields.

Calculation of perturbed orbits and physical mechanism behind observed losses

The linear MHD analysis of a well constrained equilibrium, as we have shown with SXR measurements, provides a

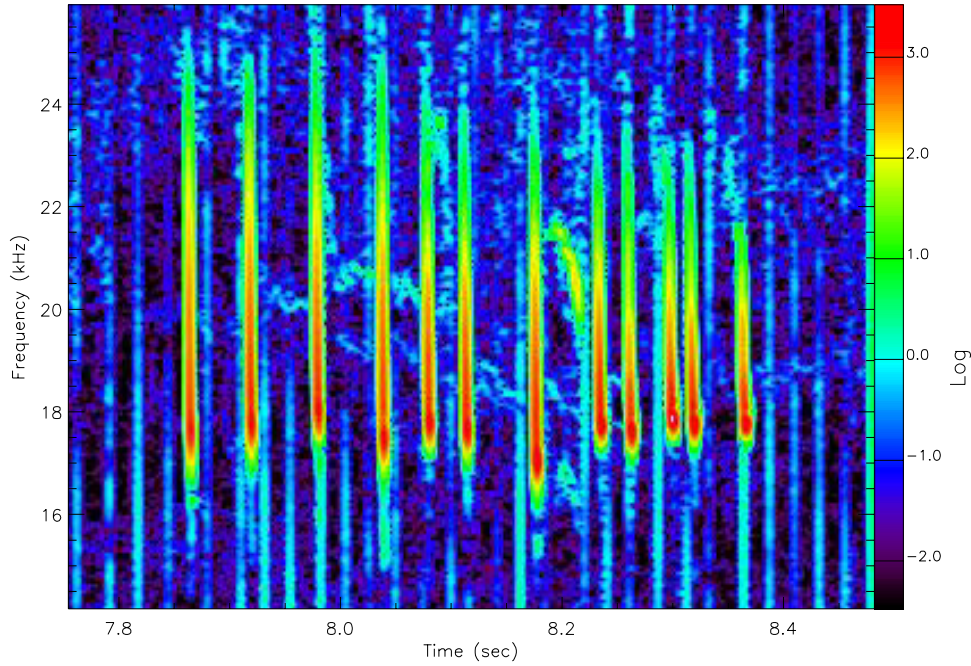


Figure 15. Fourier spectrum from magnetic pickup coils showing fishbone frequency chirping in discharge #92394.

satisfactory description of the spatial structure of the mode, but does not supply all required information; namely the amplitude of the mode and the mode frequency.

The mode frequency governs the electric field and is responsible for the change in the particle energy, since magnetic perturbations do no work. The necessary condition for resonant interaction of a drift orbit with the $n = 1$ fishbone is given by the resonance condition

$$\omega + \langle \dot{\phi} \rangle + p\omega_b = 0 \quad (5)$$

where ω_b is the poloidal bounce frequency and $\langle \dot{\phi} \rangle$ is the bounce averaged toroidal frequency. The average toroidal frequency is the sum of both the precessional and transit contributions to the motion, the relative contribution depending on the orbit topology. It is important to note that the orbits of the fusion products have poloidal bounce and bounce-averaged toroidal frequencies much larger than the frequency of the fishbone, except for a minority near the trapped/passing boundary. The non-resonant orbits behave as test particles undergoing quasi-linear diffusion rather than convection.

The frequency evolution of the fishbones as measured with magnetic probes is given in figure 15. The fishbones chirp downward in frequency from 25 kHz to 16 kHz in the lab frame. The latter frequency corresponds very well to measurements of the core plasma rotation obtained from charge-exchange spectroscopy, the large rotation owing to the strong beam heating in this high-performance pulse. The initial normalized linear growth rate is measured at $\frac{\gamma}{\omega} \approx 3\%$, which for TAEs will give a saturation amplitude of order $\frac{dB_t}{B_0} = 0.1\%$. However, the rapid frequency chirp to nearly zero frequency in the plasma frame suggests a strongly nonlinear mode which can access more energy in the distribution function, resulting in a larger amplitude. In the absence of more direct measurement

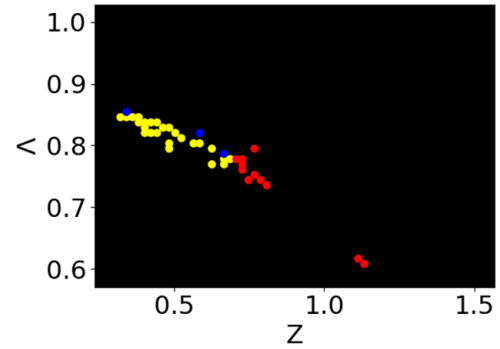


Figure 16. HALO full-orbit calculations showing the difference between two plots of orbit classification of particles, one with and the other without the fishbone, colouring as before.

of amplitude, we assumed the large value $\frac{dB_t}{B_0} = 1\%$. Much beyond this value, the fishbone becomes comparable to the equilibrium poloidal field and the plasma is likely to disrupt, so this is the largest order-of-magnitude estimate that we expect to be reasonable.

Taking the bottom of the frequency chirp to be the plasma rotation frequency, we inferred the mode frequency in the plasma frame to be 9 kHz. The modes lasted for 3 ms in total, with a mode envelope sufficiently slow as to justify neglecting its additional contribution to the electric field. The mode was therefore taken as a constant 9 kHz for a full 3 ms to give a larger estimate of perturbation to particle orbits. The MISHKA eigenvalue was discarded in equation (3) and replaced with the measured frequency to obtain the linear electric field.

The presented linear model for the fishbone was included in both the HAGIS and HALO codes and the orbits reclassified after perturbation. The perturbed orbit topology was obtained by constructing a similar graph to figure 12. Subtracting the unperturbed graph from the perturbed graph results in a plot

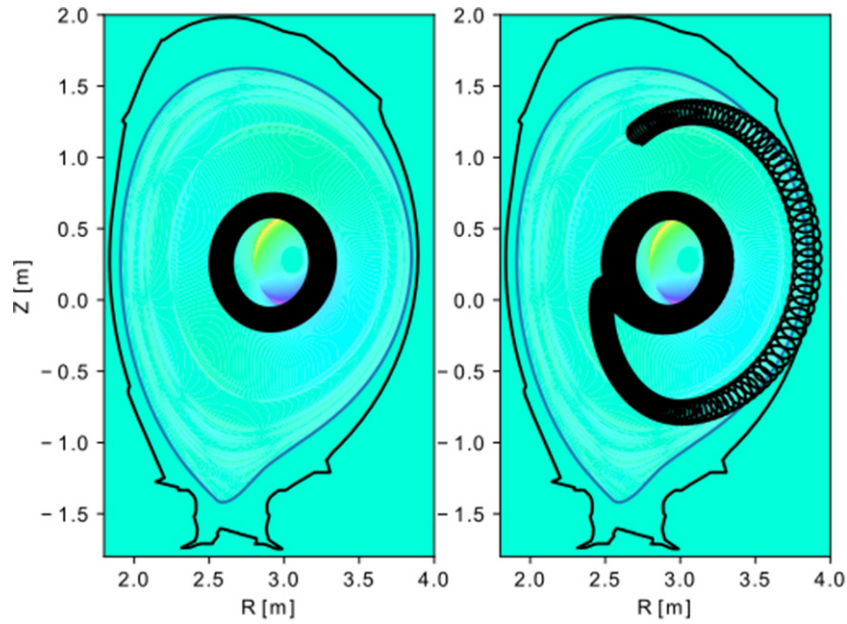


Figure 17. HALO calculation of a critical orbit undergoing topology change in the presence of a fishbone. Unperturbed (left) and perturbed (right) are shown superimposed on electrostatic potential.

of where the orbit character changed due to the fishbone (figure 16).

Both the drift (omitted) and full-orbit calculations show a very small region in phase space near the topological boundary where the fishbone changes the orbit character to create a loss. For orbits in this region of phase space, the toroidal orbit frequencies for the lost counter-passing fusion products are calculated with HAGIS to be over 500 kHz, and the trapped orbits have frequencies in the tens of kHz, both too fast to resonate with the fishbone.

The confinement of particles may be understood in terms of the invariants of motion. We consider each invariant E, μ, P_ϕ in turn, starting with μ . At low frequencies ignoring FLR effects, theory predicts magnetic moment μ to remain conserved. Drift calculations thus assume the fishbone to have no effect on magnetic moment. Conversely, in our full-orbit calculations which do not depend on the value of μ in any way, the fishbone is sufficiently narrow as to vary significantly over a Larmor radius, leading to a calculated violation of μ , however the violation in the lowest order μ was found to be periodic and did not accumulate. We do not know if this would be improved with higher order expressions of μ because the length scale of the perturbation is much shorter than the Larmor radius and an asymptotic expansion seems unjustified.

Both for drift calculations which assume exact μ conservation and for full orbit calculations which did not, a simple translation of a particle in Z due to perturbation from the fishbone was found to be the mechanism for the loss of confinement, either through topology change from passing to lost, or by simply shifting the position of a confined trapped orbit into a loss region.

The calculations showed that the proportional energy change of the particle was small compared with the change in radial position. This may be understood from the well-known invariant

$$K \equiv E - \frac{\omega}{n} P_\phi (+Z_{R=R_0}). \quad (6)$$

The break in toroidal symmetry is responsible for the change in canonical momentum, but only the induced electric field produces a proportional change in the particle energy through the frequency. Because the frequency is low, the change in energy due to the perturbation is a small proportion of the total energy of the particle. Moreover, only a small change in canonical momentum (i.e. a small change in Z) is required to create a loss.

The combination of μ and E conservation leads to Λ being well conserved in the drift calculations. The result is that the difference plot in figure 16 clearly follows the location of the boundary in figure 12.

To illustrate the typical orbit for fishbone losses, we have run HALO for one of the critical orbits near the triple point in the presence of a perturbation (figure 17). The wall is plotted in the figure but disabled in the tracking for this plot. The fishbone induced loss orbit clearly corresponds to the barely confined guiding centre orbits shown earlier.

The presented calculations of non-resonant fusion product particle motion in the presence of experimentally constrained fishbones predict wall and fast ion loss detector impact locations in agreement with those observed in experiment.

Our findings suggest that the volume of phase space sensitive to this effect is small and could not plausibly account for a significant heat loading.

Calculations of heat loads

In this section, we present calculations of the heat losses through the separatrix based on nominal fusion product sources obtained from the TRANSP code. Our purpose is to confirm our reasoning that fishbones do not affect sufficient

Table 1. HAGIS calculations of particle losses assuming an initial distribution given by TRANSP.

	Equilibrium (%)	With fishbone (%)	Difference (%)
Protons			
Confined	94.7	94.3	
Lost	5.29	5.70	0.4
Alphas			
Confined	93.3	92.4	
Lost	6.67	7.65	1

numbers of particles in the relevant region of phase space to produce losses much beyond those already occurring in stable axisymmetric equilibrium. TRANSP is used frequently on JET for scenario development, interpretive modelling and fusion product studies [23, 24]. To approximate a realistic fusion product source distribution function in our calculations, we assumed an isotropic distribution of the form

$$f(\rho, E, \lambda) \approx \frac{1}{2} \delta(E - E_0) \text{PFI}(\rho) \quad (7)$$

where the fusion power density profile ‘PFI’ was obtained from a JET TRANSP run for similar shot 92395. Calculations of power losses were performed using HAGIS with and without fishbones for both 3 MeV protons and 3.5 MeV alpha particles.

The alpha particle calculations correspond to slightly different orbit topologies than those presented, but for brevity we omit those test particle orbits here. The slightly higher energy works to increase the number of losses in comparison to the D–D fusion products, due to the larger orbit widths and Larmor radius.

The results of the HAGIS calculations using the TRANSP radial profile is given in table 1. The majority confined fraction is to be expected since the profile is used as an energy source in the energy balance calculations in TRANSP; only confined particles contribute significantly to the plasma heating. As expected from test particle orbit calculations presented earlier, the addition of the fishbone makes a tiny contribution to the overall losses in the guiding centre calculation.

Conclusions and future work

We have presented detailed calculations of the effect of fishbones on non-resonant fusion product from the D–D reaction in order to explain measured fusion product losses and to assess the likelihood that correlated main chamber hotspots are caused by the same losses. We carefully determined the radial extent of the fishbone to be localised in the core using inference of q profile and measurements from SXR cameras. The fishbone is measured to resemble the linear MHD internal kink mode structure over the entire nonlinear phase. This fundamental constraint on the localization of the fishbone immediately limits the class of particle orbits which may be ejected from the plasma. The ejection of particles is limited to those

whose orbit width plus Larmor radius exceeds the distance from the $q = 1$ rational surface to the separatrix.

The loss mechanism for fusion products can be explained as solely due to barely confined orbits diffusing in radius due to a violation of axisymmetry. The mode frequency is too low to alter the particle energy or magnetic moment significantly. The barely confined guiding centre orbits are particularly noteworthy for our study here in that our calculations show that they impact the wall where the hotspots are observed in experiment.

This orbit-width is a function of the poloidal Larmor radius and will therefore be a function of the plasma current and device dimension. On JET, non-resonant particles in the *MeV* range satisfy that criterion but resonant NBI injected particles do not. On ITER, the linear dimensions and current are sufficient to discount any fishbone induced loss of particles, although we do not make any claims about redistribution, which could be significant; large fishbones clearly lead to stochastic diffusion of non-resonant particles.

Having understood the mechanism and class of particles ejected according to drift and full-orbit calculations, we loaded a realistic particle distribution of fusion products over the full phase space to give quantitative estimates for heat loads. Our conclusion was that the large fishbones observed account for a mere $\sim 1\%$ power loss even when considering the alpha particles in the same conditions.

The conservation of magnetic moment is absolutely crucial in confining fusion products in this JET shot. Consider again figure 13; the combination of wall proximity and large Larmor radius means that losses occur for any radius but only certain values of pitch angle. If pitch angle scattering could occur on timescales faster than slowing down timescales, loss rates of fusion products would be proportional to the rate of pitch angle scattering. Higher frequency modes are expected to be capable of such scattering and may warrant increased attention for their effects on non-resonant fusion products in low current scenarios.

Acknowledgments

This work has been carried out within the framework of the EUROfusion Consortium and has received funding from the Euratom research and training programme 2014–2018 under grant agreement No 633053 and from the RCUK Energy Programme (grant number EP/P012450/1). To obtain further information on the data and models underlying this paper please contact PublicationsManager@ccfe.ac.uk. The views and opinions expressed herein do not necessarily reflect those of the European Commission.

ORCID iDs

S.E. Sharapov  <https://orcid.org/0000-0001-7006-4876>

References

- [1] Gormezano C., Challis C.D., Joffrin E., Litaudon X. and Sips A.C.C. 2008 Advanced tokamak scenario development at JET *Fusion Sci. Technol.* **53** 958–88
- [2] Kiptily V.G. et al 2018 Fusion product losses due to fishbone instabilities in deuterium JET plasmas *Nucl. Fusion* **58** 014003
- [3] von Thun C.P. et al 2010 MeV-range fast ion losses induced by fishbones on JET *Nucl. Fusion* **50** 084009
- [4] Porcelli F. 1991 Fast particle stabilisation *Plasma Phys. Control. Fusion* **33** 1601–20
- [5] Chen L., White R. and Rosenbluth M.N. 1984 Excitation of internal kink modes by trapped energetic beam ions *Phys. Rev. Lett.* **52** 1122–5
- [6] Coppi B. and Porcelli F. 1986 Theoretical model of fishbone oscillations in magnetically confined plasmas *Phys. Rev. Lett.* **57** 4–7
- [7] McGuire K. et al 1983 Study of high-beta magnetohydrodynamic modes and fast-ion losses in PDX *Phys. Rev. Lett.* **50** 891–5
- [8] Wesson J.A. 1978 Hydromagnetic stability of tokamaks *Nucl. Fusion* **18** 87–132
- [9] de Blank H.J. 1990 Theory of the $m = 1$ Kink Mode in Toroidal Plasmas *PhD Thesis* Rijksuniversiteit Utrecht (https://inis.iaea.org/search/search.aspx?orig_q=RN:22006377)
- [10] Bussac M., Pellat R., Edery D. and Soule J. 1975 Internal kink modes in toroidal plasmas with circular cross sections *Phys. Rev. Lett.* **35** 1638–41
- [11] Waelbroeck F.L. and Hazeltine R.D. 1988 Stability of low-shear tokamaks *Phys. Fluids* **31** 1217
- [12] Hastie R.J. and Hender T.C. 1988 Toroidal internal kink stability in tokamaks with ultra flat q profiles *Nucl. Fusion* **28** 585
- [13] Manickam J., Pomphrey N. and Todd A.M.M. 1987 Ideal MHD stability properties of pressure driven modes in low shear tokamaks *Nucl. Fusion* **27** 1461–72
- [14] Baeumel S. et al 2004 Scintillator probe for lost alpha measurements in JET *Rev. Sci. Instrum.* **75** 3563–5
- [15] Brix M., Hawkes N.C., Boboc A., Drozdov V. and Sharapov S.E. 2008 Accuracy of EFIT equilibrium reconstruction with internal diagnostic information at JET *Rev. Sci. Instrum.* **79** 10F325
- [16] Heidbrink W. and Sadler G. 1994 The behaviour of fast ions in tokamak experiments *Nucl. Fusion* **34** 535–615
- [17] Baruzzo M. et al 2010 Neoclassical tearing mode (NTM) magnetic spectrum and magnetic coupling in JET tokamak *Plasma Phys. Control. Fusion* **52** 75001
- [18] Mikhailovskii A., Huysmans G., Kerner W.O.K. and Sharapov S.E. 1997 Optimization of computational MHD normal-mode analysis for tokamaks *Plasma Phys. Rep.* **23** 844–57
- [19] Wang F., Fu G.Y., Breslau J.A. and Liu J.Y. 2013 Linear stability and nonlinear dynamics of the fishbone mode in spherical tokamaks *Phys. Plasmas* **20** 102506
- [20] O’blom A., Breizman B.N., Sharapov S.E., Hender T.C. and Pastukhov V.P. 2002 Nonlinear magnetohydrodynamical effects in precessional fishbone oscillations *Phys. Plasmas* **9** 155
- [21] Breizman B.N. and Sharapov S.E. 2011 Major minority: energetic particles in fusion plasmas *Plasma Phys. Control. Fusion* **53** 54001
- [22] Pinches S.D. et al 1998 The HAGIS self-consistent nonlinear wave-particle interaction model *Comput. Phys. Commun.* **111** 133–49
- [23] Budny R.V. et al 2000 Local transport in Joint European Tokamak edge-localized, high-confinement mode plasmas with H, D, DT, and T isotopes *Phys. Plasmas* **7** 5038–50
- [24] Weisen H. et al 2017 The ‘neutron deficit’ in the JET tokamak *Nucl. Fusion* **57** 076029
- [25] Litaudon X. et al 2017 *Nucl. Fusion* **57** 102001